Volume 5 | Number 23 | 21 June 2017 | Pages 11367–11962

Journal of Materials Chemistry A

Materials for energy and sustainability

rsc.li/materials-a

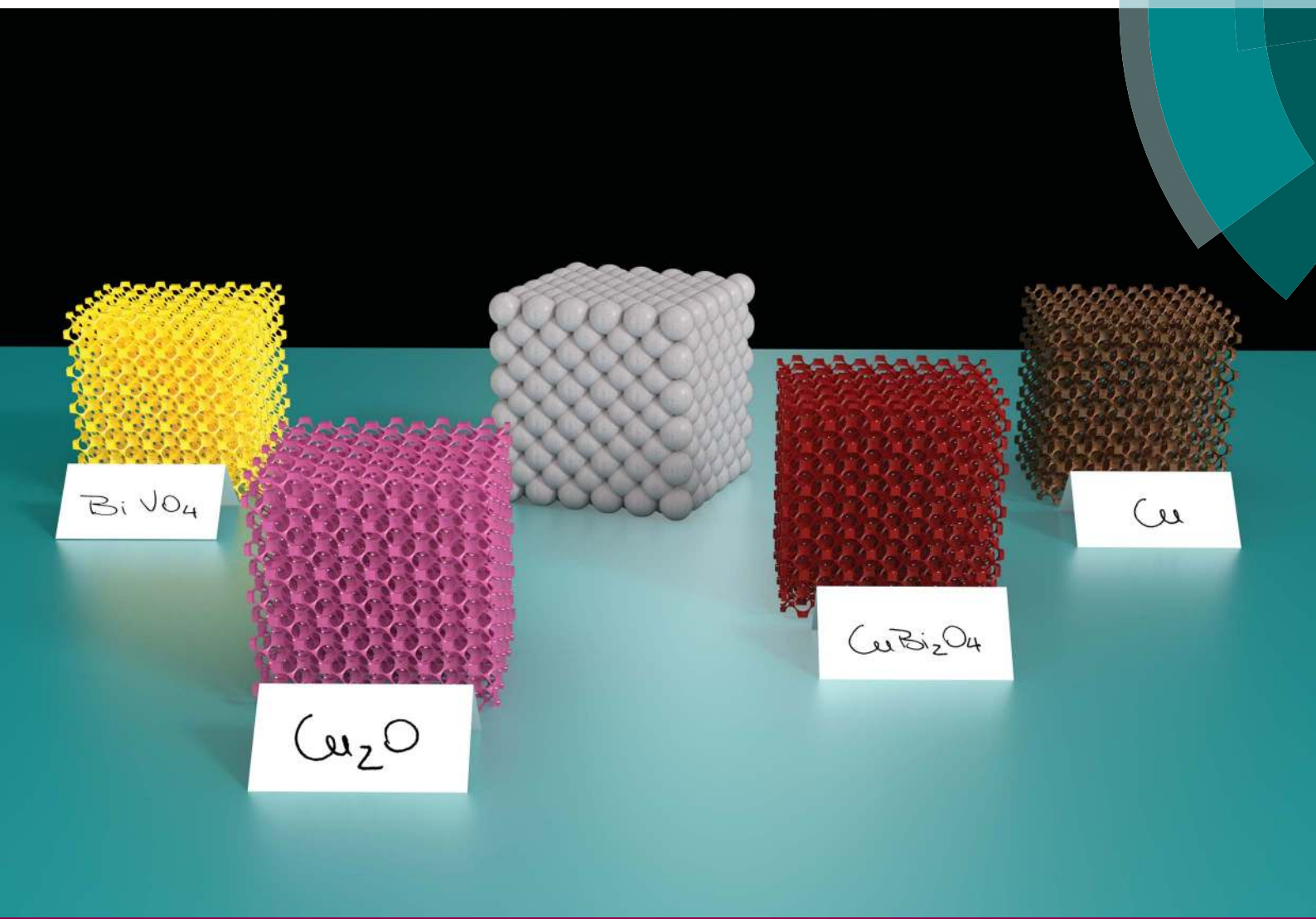

Themed issue: Emerging Investigators 2017

ISSN 2050-7488

ROYAL SOCIETY OF CHEMISTRY

PAPER

F. M. Toma *et al.*

Fabrication and optical characterization of polystyrene opal templates for the synthesis of scalable, nanoporous (photo)electrocatalytic materials by electrodeposition

Journal of Materials Chemistry A

PAPER

View Article Online
View Journal | View Issue

Cite this: J. Mater. Chem. A, 2017, 5, 11601

Fabrication and optical characterization of polystyrene opal templates for the synthesis of scalable, nanoporous (photo)electrocatalytic materials by electrodeposition†

E. A. Gaulding,[ab] G. Liu,[ab] C. T. Chen,[c] L. Löbbert,[ab] A. Li,[ab] G. Segev,[ab] J. Eichhorn,[b] S. Aloni,[c] A. M. Schwartzberg,[c] I. D. Sharp[ab] and F. M. Toma*[ab]

Received 16th January 2017
Accepted 2nd March 2017

DOI: 10.1039/c7ta00512a

rsc.li/materials-a

Finding solutions to improve the performance of semiconductor light absorbers and catalyst materials remains an outstanding issue that prevents the realization of solar fuel generators. Nanostructuring approaches of photoelectrocatalytic materials have the potential to reduce bulk recombination and improve electron–hole pair separation in semiconductor light absorbers, as well as to increase the active surface area and influence the activity in catalytic systems. Herein, we propose a versatile approach for the synthesis of reproducible, highly homogeneous, large scale nanoporous (photo)electrocatalytic materials for artificial photosynthesis. By identifying and carefully analyzing critical parameters for forming opal templates from solutions of colloidal polystyrene beads (PS), we are able to reproducibly fabricate large area (>cm^2) PS films with high optical quality over a wide diameter range (170–600 nm). Using these PS bead opal films as templates, we demonstrate that electrodeposition is a suitable bottom-up infilling technique to produce scalable, homogeneous, and highly ordered nanoporous (photo)electrocatalytic materials, namely Cu_2O, $BiVO_4$, $CuBi_2O_4$, and Cu. We provide morphological, structural, and optical characterization of the resulting opal replicas. Finally, we demonstrate preliminary integration of the Cu_2O inverse opal film into a working photocathode under CO_2 reduction conditions.

Introduction

The increasing use of fossil fuels to meet human energy needs has caused a steep rise of the atmospheric carbon dioxide levels and is strongly influencing climate change.[1–3] While more than 75% of the current energy supply still originates from fossil fuels, photoelectrochemical carbon dioxide reduction and H_2 production provide promise as sustainable alternatives that are well suited for the capture and direct conversion of solar energy into chemical fuels, thus addressing the central challenge associated with the intermittency of sunlight. However, realization of practical solar fuel generators is hindered by a lack of material systems and assemblies that are simultaneously efficient and cost-effective.[1]

The main components of integrated photoelectrochemical systems are semiconductor light absorbers, which often suffer from significant bulk recombination and charge transport limitations that undermine both their efficiency and stability. In this architecture, semiconductor light absorbers are coupled to catalysts, which also must provide high activity, selectivity, and stability.[4,5] The use of nanostructured photoelectrodes can decouple the light absorption depth from an unmatched charge transport length, thus providing an appealing approach to improving electron–hole pair separation and reducing bulk charge recombination.[6,7] In addition, nanostructuring of electrodes for (photo)electrochemistry can dramatically enhance efficiency by providing a high electrochemically active surface area per geometric area, promote selectivity of active sites *via* specific nanomorphology (*i.e.* selective faceting and concentration of grain boundaries), and influence catalytic site activity by altering the local geometrical environments of surface-bound chemical species in confined systems.[8]

The design and realization of (photo)electrodes with monodisperse, tunable pore sizes is key to studying the effects of surface curvature on chemical activity, mass transport of chemical reactants and products in confined systems, and competitions between chemical reactions and charge recombination at light absorber interfaces. In addition, such systems provide the possibility of generating photonic crystals for the controlled manipulation of light propagation in photoelectrodes. Unlike

[a]Joint Center for Artificial Photosynthesis, Lawrence Berkeley National Laboratory, 1 Cyclotron Road, Berkeley, California 94720, USA. E-mail: fmtoma@lbl.gov
[b]Chemical Sciences Division, Lawrence Berkeley National Laboratory, 1 Cyclotron Road, Berkeley, California 94720, USA
[c]The Molecular Foundry, Lawrence Berkeley National Laboratory, 1 Cyclotron Road, Berkeley, California 94720, USA

† Electronic supplementary information (ESI) available. See DOI: 10.1039/c7ta00512a

different synthetic approaches that result in electrodes with inhomogeneous pore sizes with little or no control over the pore diameter and size distribution,[9–11] 3-dimensional (3D) inverse opals (IOs) can be characterized by highly ordered and uniform porous structures. IOs are commonly obtained by infiltration of ordered polystyrene (PS) sphere templates, which themselves possess the characteristic properties of photonic crystals. The periodicity of IO architectures can be easily modified by changing the diameter of the polystyrene sphere template, which affects the actual pore dimension and the interconnecting space between pores. In these ordered structures, light can be scattered and diffracted depending on the periodicity and refractive index of the material, from which a photonic band gap (PBG) or photonic crystal stop band emerges. While the nanoporous interconnecting space between the pores ensures electronic connectivity, the nanostructured characteristic can help match the charge transport length with the diffusion length. In addition, the interesting optical properties of IOs can enhance light harvesting, which consequently increases the generation of electron–hole pairs. This latter enhancement is due to the slow photon effect, which describes how light propagates at the edges of the PBG. To date, a few studies have reported the benefits of using IO architectures as photoelectrochemical systems.[12,13] For example, Zhou *et al.* have described optimized charge transport properties in ordered bismuth vanadate ($BiVO_4$) photonic crystals.[14] Then, the same group has reported that the performance of $BiVO_4$ photonic crystals is inversely related to the pore and interconnecting space dimensions.[15] Examples of photonic crystal photoanodes based on tungsten oxide (WO_3) and engineered $BiVO_4/WO_3$ heterojunctions have also shown improved photocurrent with respect to their disordered and planar counterparts.[16,17] Despite these encouraging results, the range of materials and sizes of photoelectrodes fabricated in such architectures remains limited. In particular, with respect to existing reports,[14–17] we recognize the need to bridge the gap between fabricating large scale opal template films and effectively converting them into equally homogenous ordered replicas.

In order to produce uniform, large grain inverse opal films for large scale photoelectrodes that fully benefit from the emergent optical properties, low defect concentration IOs are necessary. Indeed, polycrystallinity and disorder in the crystal can affect periodicity and attenuate the photon mean free path in defective IOs.[18,19] For example, Ozin and collaborators have provided evidence that the lower the disorder the higher the photocatalytic degradation of organic dyes in TiO_2 photonic crystals.[20] In addition, cost-effective, reproducible, and versatile synthetic methods that match the required structural quality are also needed.

For operation as a working electrode, the ultimate inverse opal structure needs to uniformly cover the substrate surface. This stringent requirement strongly depends on obtaining highly ordered PS bead templates and on maintaining significant homogeneity over cm^2 areas. In addition, the synthesis of high-quality nanostructured (photo)electrocatalytic opal replicas calls for a bottom-up infilling approach that can retain the high homogeneity of the original template over large scales, while being amenable to the deposition of different materials. Most importantly, the material of interest should grow from the substrate outwards during infilling, thereby ensuring electrical contact and continuity of the deposited material. Electrodeposition is a bottom-up solution-based synthesis compatible with ambient conditions that in recent years has been widely used for producing various planar highly efficient (photo)electrodes for solar fuel production, including metals,[21] alloys,[22] oxides,[23] chalcogenides,[24] and III–V semiconductors.[25] While the viability of this method to infill PS opal templates has been proven,[26–28] infilling opal templates specifically with semiconductor photoelectrode materials by electrodeposition has not been widely explored. Notably, to the best of our knowledge, there is no reported example of highly homogeneous, large scale inverse opal photonic crystal photoelectrocatalytic materials synthesized with this approach. For example, while a few studies have been recently reported for the fabrication of Cu_2O nanoporous structures through templates of colloidal beads by electrodeposition, the pore arrangement was either amorphous[27] or the grain size/area of ordered porous structures was small.[28,29] A Cu_2O photonic crystal has been successfully formed by electrodeposition through a photoresist template patterned *via* multibeam interference lithography.[30] However, the use of this technique requires an expensive, complex setup and is difficult to scale up. High-quality, large area inverse opal structures of Cu_2O that exhibit the photonic effect have yet to be synthesized *via* simple solution techniques. Similarly, while examples of $BiVO_4$ photonic crystals obtained by sol–gel methods have already been reported to successfully improve the efficiency of the material,[14,31] these approaches do not allow for the fabrication of large area electrodes and typically require multiple cycles to completely infill the space between the template.

Herein, we report the detailed synthesis of scalable (cm^2), highly reproducible PS opal templates for the fabrication of electrodeposited IOs of (photo)electrocatalytic materials (Scheme 1). With respect to the existing synthetic methods for PS opal templates,[32,33] we find that fabrication of high optical quality films over cm^2 areas requires control over multiple parameters, namely substrate surface hydrophilicity, tilt angle, temperature, humidity, solvent, and added surfactant. We provide a detailed analysis of the role of these parameters that contribute to achieving a balance between highly ordered beads on the micrometer scale while maintaining homogeneity on the macro scale. Fine tuning these experimental knobs allows synthesis of high-quality PS opal films not only over cm^2 areas, but also over a wide range of bead diameters, from 170 to 600 nm. The high quality of these PS opal templates is confirmed *via* optical transmission and reflectance measurements, where a strong and sharp photonic crystal stop band is observed. In addition, full-wave simulation of the optical response of PS opal template analogues supports the experimental results, and confirms the presence of a red-shift of the photonic crystal stop band due to the increasing size of the PS beads. Then, these high-quality substrates are used to template bottom-up electrodeposition of IO porous structures comprising a variety of electrocatalytic and photoelectrocatalytic materials of interest for artificial photosynthesis. These materials span photoelectrodes and dark catalysts, such as cuprous oxide (Cu_2O), bismuth vanadate ($BiVO_4$),

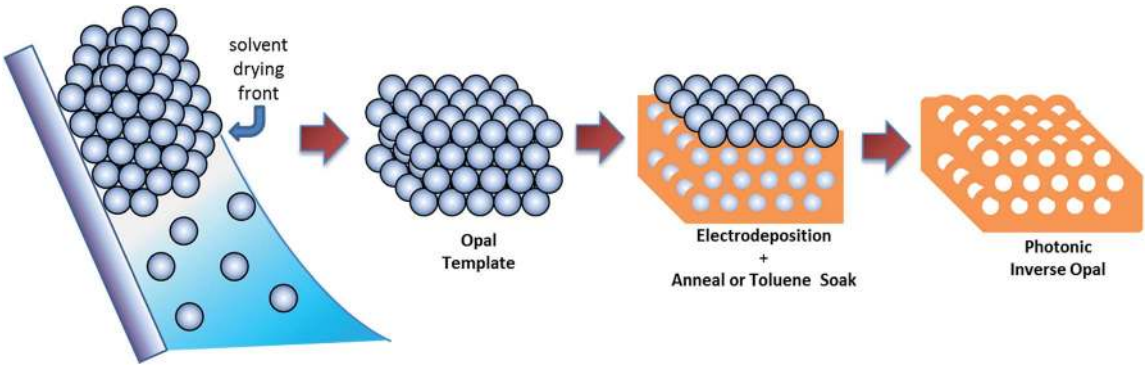

Scheme 1 Schematic illustration of the polystyrene opal and inverse opal fabrication process.

copper bismuth oxide ($CuBi_2O_4$), and copper (Cu). Notably, the electrodeposition of $BiVO_4$ or $CuBi_2O_4$ *via* PS opal templating has not been investigated. In addition, no reported example of a $CuBi_2O_4$ IO structure has yet been reported. The quality of the obtained inverse opals is assessed by morphological, optical, and structural characterization. In addition, to the best of our knowledge for the first time, initial functional photoelectrochemical performance properties of Cu_2O IOs under aqueous CO_2 reduction conditions are shown. Thus, we demonstrate that this approach provides a promising, universal methodology for the production of IO materials with high periodicity and with pore size control over areas relevant for application as functional (photo)electrodes.

Experimental

Materials

Non-functionalized polystyrene beads of sizes 400, 500, and 600 nm (25 mg mL^{-1} in water) were purchased from Corpuscular; beads of sizes 200, 350, and 510 nm (Polybead® Microspheres, 2.5% w/v in water) were purchased from Polysciences; beads of sizes 170, 280, and 390 nm (10% w/w in water) were purchased from Bangs Labs. Water (18.2 MΩ cm, at 25 °C) was used as a solvent and dispensed from an EMD Millipore system (Milli-Q® Integral Water Purification System). Ethanol (>99.5%), acetone (99.9%), hydrochloric acid (37%), nitric acid (70%), TritonX, copper sulfate (>98%), lactic acid (85%), vanadium(IV) oxysulfate hydrate (97%), copper nitrate (>99%), bismuth nitrate (>98%), sodium acetate trihydrate (99.5), sodium hydroxide (98%), and fluorine doped tin oxide (FTO, TEC 15, 13.2 nm roughness) glass with a surface resistivity of ~13 Ω sq^{-1} were purchased from Sigma-Aldrich. Toluene (>99.5%) and 1 mm thick fused silica were purchased from VWR. Cu foil (0.127 mm thick, 99.9%, 26.0 nm roughness) was purchased from Alfa Aesar. All materials and chemicals were used as received unless otherwise stated.

Deposition of polystyrene opal films

To fabricate large area, cm^2 scale PS opal templates over a wide diameter range of PS spheres, 1 × 2 cm^2 FTO and quartz substrates were first made hydrophilic by using the following cleaning procedure: (1) substrates were sonicated in an Alconox/DI water solution for 15 min, (2) then sonicated in pure DI water for 15 min, and (3) next sonicated in a 1 : 1 : 1 acetone, ethanol, and DI water solution for 15 min. Finally, the substrates were treated with air plasma for ~5 min. Between each step, the substrates were inspected for dust/particulates which were removed *via* a combination of physical agitation with Kimwipes and flowing nitrogen, as necessary. For the Cu inverse opals, thin 1 × 2 cm^2 copper sheets were used as the substrate, as Cu poorly adheres to FTO. The cleaning procedure was the same as for the FTO except that the plasma treatment was substituted with a brief wash in 4 M HCl.

PS bead solutions were diluted from their stock solutions to between 0.05 and 0.4 v/v%, depending on the size of the PS beads. Millipore water was used consistently as the solvent for the PS bead deposition. For solutions with bead diameters ≥400 nm, a few drops of a 1% solution of TritonX were added. PS bead solutions were sonicated for 15 min before deposition. For a detailed table of the dilution concentrations and added surfactant amounts for each individual PS bead size, please refer to the ESI (Table S1†).

The substrates were set tilted at a 60° angle (where 0° is flat horizontal) with each sample placed individually in small vials (1.5 cm diameter and 4.5 cm height). 1.5 mL of the desired PS bead solution was carefully dispensed into the vials by applying the pipette tip to the edge of the vial. The vials were arranged in a 4 × 4 grid on a hotplate for a total of 16 vials. The hotplate was then covered with a crystallization dish (15.0 cm diameter and 7.5 cm height) with a filter paper taped to the bottom so that droplets did not fall into the vials as water re-condensed on the glass. The hotplate was then set to the desired temperature (see Table S1† in the ESI for details per PS bead size). The humidity and evaporation rate were reproduced by always maintaining the same amount of water in the enclosed system (*i.e.* if only making 8 substrates, the other 8 vials were still filled with 1.5 mL of water). Depending on the temperature, the deposition was complete after 1–4 days.

After the deposition, the films with bead sizes ≥400 nm were immersed in ethanol for 1 h, and then removed and carefully dried using a gentle stream of nitrogen on the back side of the substrate. This "solvent annealing" step improves the crystallinity and therefore optical properties of the PS opal (Fig. S1†).

All substrates were annealed on a hotplate at 90 °C for 10 min to remove any remaining solvent and ensure good contact of the beads with themselves and the substrate.[34,35]

Simulation of the optical response of polystyrene opal films

Finite difference time domain calculations of the optical response of PS opal films were performed using Lumerical FDTD Solutions. The experimentally realized films were approximated with a three-dimensional face-centered cubic (FCC) opal structure 20 layers thick on top of a SiO_2 slab. Commonly available wavelength-dependent refractive indices for the PS[36] and SiO_2 (ref. 37) were used. The simulation area was defined by periodic boundaries encompassing a single FCC supercell in the lateral directions and perfectly matched layer absorbing boundaries in the vertical directions. Transmission and reflection were calculated from frequency domain field and power monitors placed below the structure in the SiO_2 slab and above the structure and the plane wave source respectively.

PS template electrode preparation

Substrates were prepared for electrodeposition by contacting the bare substrate edge with copper tape (Ted Pella, 16074), and then carefully constructing a window (0.7–1.2 cm^2 area) out of electrochemical tape (VWR, 33725-513) to mask off all area except where the PS opal film was present. Just before conducting the actual electrodeposition, a drop of ethanol was wicked onto the electrode window and the substrate was then gently immersed into the electrodeposition solution without agitation. This step helped prevent delamination of the film and promoted penetration of the solution into the PS template. A standard three-electrode cell comprising a FTO working electrode, a Ag/AgCl (3 M NaCl, BASI) reference electrode, and a platinum counter electrode was used for electrodeposition. In a typical deposition, approximately 50 mL of chemical bath solution was used.

Electrodeposition of Cu_2O

Deposition of Cu_2O was adapted from a previous literature procedure.[38] In a typical experiment, a 0.4 M $CuSO_4$ solution was prepared by stirring 4.99 g $CuSO_4$ in 25 mL of Millipore water. 13.51 g of lactic acid was added, and then 3 M NaOH was added dropwise to the solution until it stabilized at pH 9. The solution was then diluted by half to produce a 0.2 M $CuSO_4$ solution and adjusted to pH 9 by adding a few more drops of the 3 M NaOH. Cu_2O was deposited on the substrate under chronoamperometric conditions at −0.3 V *vs.* Ag/AgCl at 55 °C. The deposition was done in five 10 min cycles (50 min total) to monitor the film thickness and allow diffusion of the solution since it was not stirred so as to not agitate the template. After the deposition, the substrates were gently rinsed with water and then with ethanol, and finally gently dried with a nitrogen gun. Next, the PS beads were removed by cycling between toluene/acetone rinses. This procedure successfully yielded electrodeposited cubic cuprite Cu_2O through the PS template on FTO. A planar film for optical characterization was also deposited on FTO without the presence of PS beads using the same conditions.

Electrodeposition of $BiVO_4$

$BiVO_4$ electrodes were prepared *via* an electrodeposition procedure for planar films adapted from the literature.[39] In brief, 10 mM $Bi(NO_3)_3$ was added after the pH of 35 mM $VOSO_4$ solution reached <0.5 by the addition of HNO_3. To stabilize the otherwise insoluble Bi(III) ions at mildly acidic pH, 2 M sodium acetate was added, raising the pH to 5.1, which was then adjusted to pH 4.7 with HNO_3. Deposition of amorphous Bi–V–O films was carried out potentiostatically at 1.9 V *vs.* Ag/AgCl between 45 min and 1.5 h at 55 °C. All freshly prepared films were gently rinsed with water and then ethanol, and then gently dried with a nitrogen gun. The films were then annealed at 500 °C for 1 h in air with a 2 °C per minute ramping rate. After annealing, the as-prepared films were soaked in 1 M NaOH with stirring for 20 min to remove the excess V_2O_5 and yield phase pure monoclinic scheelite $BiVO_4$. A planar $BiVO_4$ film for optical characterization was deposited on FTO without the presence of PS beads with similar deposition conditions and a deposition time of 5 min.

Electrodeposition of $CuBi_2O_4$

$CuBi_2O_4$ was formed through a PS bead film on FTO *via* electrodeposition and annealing conditions adapted from the previously reported recipe for planar films described by Mullins *et al.*[40] Specifically, we used a 4 mM $Cu(NO_3)_2$ and 8 mM $Bi(NO_3)_2$ in 10% nitric acid solution as the chemical bath. The electrodeposition of $CuBi_2O_4$ was carried out at a constant potential (−0.7 V) for 5 min. Substrates were carefully rinsed with water and then ethanol, and then gently dried with a nitrogen gun after electrodeposition. The PS beads were removed during the annealing step in air (600 °C, 2 h, 2 °C min^{-1} ramp rate) for the formation of crystalline tetragonal kusachiite $CuBi_2O_4$.

Electrodeposition of copper

Copper was deposited by adapting the deposition procedure for Cu_2O, and using a PS opal template on a thin Cu sheet as the working electrode. A 0.4 M $CuSO_4$ solution in lactic acid (pH 9) was used as the electrochemical bath, and Cu was deposited on the substrate under chronoamperometric conditions at −0.7 V for 50 min. The PS beads were removed by cycling between toluene/acetone rinses to yield FCC copper porous substrates.

UV/Vis/NIR transmission and reflectance measurements

Transmission and spectral reflectance measurements were performed on a Shimadzu SolidSpec-3700 UV/Vis/NIR spectrometer using an integrating sphere. The baseline for the reflectance measurement was collected with a silver mirror (Thor Labs PF10-03-P-01). All measurements used an aperture with a 6 mm spot size.

Angle dependent reflectance measurements

The angle dependent reflectance measurements were taken at angles 45–80 degrees from the substrate normal vector in 5 degree increments with equal incident and receiving angles

using a M-2000 ellipsometer with an extended NIR range by J. A. Wollam Co., Inc (Lincoln, NE, USA).

Scanning electron microscopy

Scanning electron microscopy (SEM) imaging was performed on an FEI Quanta 250 FEG microscope with an acceleration voltage of 5–10 keV and 10 mm working distance.

Atomic force microscopy

Atomic force microscopy (AFM) measurements were performed under ambient conditions using a Bruker Dimension Icon AFM. For all measurements, a rectangular silicon cantilever (RFESP-75, Bruker) with a spring constant of 2.8 N m^{-1} was used. Topography images of the surface were acquired in peak force (PF) tapping mode at 2 kHz modulation with a PF amplitude of 150 nm. The linear scan rate was set to 0.3–0.5 Hz. The AFM data were processed with Gwyddion (free scanning probe microscopy data analysis software) by line alignment and plane leveling.

X-ray diffraction

Wide angle XRD was performed on a Rigaku Smartlab system equipped with a Cu source using BB or PB/PSA modes.

Photoelectrochemical measurements

All photoelectrochemical measurements were performed using a BioLogic SP300 potentiostat in a three-electrode photoelectrochemical cell with a planar quartz window (5 cm^2). Cuprous oxide photocathodes were configured as the working electrodes, a coiled Pt wire as the counter electrode, and an Ag/AgCl (3 M NaCl, BASI) as the reference electrode. Measurements were performed in 0.1 M $KHCO_3$ electrolyte saturated with Ar (pH 7.2) or with CO_2 (pH 6.8). All measurements under illumination were performed using simulated AM 1.5 light (Solar Light) adjusted to 100 mW cm^{-2} using a calibrated Si photovoltaic cell (SolarSim calibration, Newport). Photoelectrochemical performance was established by running CVs from the open circuit potential (E_{oc}) to −0.094 V *versus* the RHE (−0.7 V *vs.* Ag/AgCl) at a scan rate of 50 mV s^{-1}. Both dark and illuminated cyclic voltammograms (CVs) were collected.

Incident photon-to-current efficiency (IPCE) measurements

IPCE measurements were carried out using a Newport 300 W Ozone free Xe lamp where the optical output was passed through an Oriel Cornerstone 130 1/8m monochromator. In order to reduce light induced degradation, the lamp power was reduced to 150 W. The sample current was measured with a Gamry Reference 600 potentiostat. Cuprous oxide photocathodes were configured as the working electrodes, a coiled Pt wire as the counter electrode, and an Ag/AgCl (3 M NaCl, BASI) as the reference electrode. Measurements were performed in 0.1 M $KHCO_3$ electrolyte saturated with CO_2 (pH 6.8) at an applied bias of −0.29 V *vs.* Ag/AgCl (0.3 *vs.* RHE). The monochromatic light was stepped in 10 nm intervals and chopped at a period of 8 seconds in which the sample was illuminated only in the first 4 seconds of each period. The current under illumination was calculated by averaging readings in the last second of the illuminated interval. The dark currents were calculated by averaging the last second of the non-illuminated interval in every period. The photocurrent was calculated by reducing the dark current from the current under illumination at each cycle. The incident optical output at each wavelength was measured with a Newport 71648 photodiode.

Results and discussion

Control of parameters affecting the deposition of homogeneous, scalable PS templates

The prerequisite to fabricate inverse opal films for large scale photoelectrodes is to obtain high-quality highly ordered PS bead templates over cm^2 areas. In an attempt to deposit such homogeneous PS templates, we have found that several parameters have a significant impact on the PS bead assembly and film homogeneity. Therefore, we provide a rigorous study and understanding of the roles of solvent, added surfactant, surface hydrophilicity, tilt angle, temperature, and humidity in the assembly process.

With the goal of producing photonic IO materials, we have chosen slow evaporation as the assembly method for the PS beads over a range of diameters from 170 to 600 nm. This method allows the formation of thick, highly ordered PS opals with a strong photonic effect. In contrast, other methods produce thinner opal layers, as in the case of dip-coating,[41] or opal structures with smaller crystalline grains, as in the case of spin-coating.[42] For the case of PS opal formation by the slow evaporation method, ethanol[43] and water[32] are commonly used as solvents. However, we have found that while films deposited from ethanol are uniform, the PS beads are only moderately ordered and the photonic crystal stop band is weak (Fig. S2†). On the other hand, initial trials using water as the solvent resulted in highly ordered PS beads, but deposited in bands across the substrate, thereby yielding inhomogeneous templates (Fig. S3†). This solvent strike-slip phenomenon, commonly known as the "coffee ring effect", is caused by the capillary flow at contact lines of evaporating droplets containing dispersed non-volatile solids.[44] Because in our case high order of the PS beads is crucial, we have investigated additional parameters to minimize the coffee ring effect. Adding a small amount (μL) of surfactant (TritonX) to beads with diameters ≥400 nm dispersed in water improved the overall quality of the films without negatively impacting PS assembly (Fig. 1a, S4 and S5†). In this process, the surfactant decreases the surface tension of water, ameliorating the coffee ring effect through a phenomenon known as the Marangoni effect.[45] Indeed, similar improvements of the coffee ring effect have been observed for the evaporation of water droplets containing suspended silica beads and hydrosoluble polymer additives.[46]

While the deposition solution plays a primary role in determining the quality of the film, equally important is the control of the substrate quality and its handling during the deposition. Specifically, substrate hydrophilicity is crucial to achieving good wetting of the solvent on the substrate. Therefore, in addition to a solution cleaning treatment (detailed in the Experimental

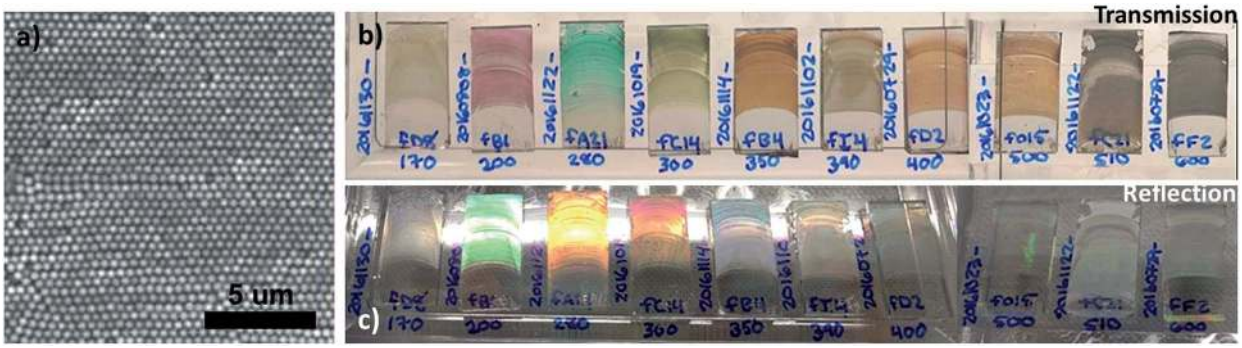

Fig. 1 (a) SEM image of a 500 nm PS bead film, (b) transmission and (c) reflection camera images of the PS templates showing film uniformity over a >1 cm^2 area. PS templates reported in (b) and (c) are 1 × 2 cm^2.

section), substrates were treated with air plasma as the final step, thereby rendering them hydrophilic and improving their wettability. In addition, the tilt angle of the substrate plays a significant role in the assembly.[47] While substrates are commonly dried vertically,[48] we find that tilting the substrates at an angle of approximately 60° during the slow evaporation process reduces the severity of the strike-slip movement of the drying front. At the same time, the substrate needs to maintain an angle (>45°) in order to ensure homogeneity of the film thickness across the substrate (Fig. S6†). Finally, both temperature and humidity of the drying environment are instrumental in determining the final quality of the PS opal film, as they control the actual evaporation rate of the water solution. In particular, under low humidity conditions, the drying rate of the films dramatically increases, ultimately affecting the opal homogeneity (Fig. S7†). Therefore, drying of these films needs to be carried out in a water saturated environment. In a typical experiment, a series of vials are dried on a single hotplate covered with a crystallization dish. The temperature and total amount of solvent within the setup are maintained constant for every experiment, fixing the temperature, humidity, and, ultimately, the evaporation rate of the solvent as the films form. The details of all the parameters mentioned above for each bead size can be found in the Experimental section. The opal film thickness is dependent on the solution concentration and can be varied from a monolayer to tens of layers (Fig. S8†). Control over the PS film thickness is important to prevent electronic transport limitations during the electrodeposition process, thus preventing a successful synthesis of the (photo)electrocatalytic materials. Typical films assembled from 500 nm beads are about 3 μm thick (Fig. S8†). In summary, by controlling the substrate tilt angle, surface hydrophilicity, solvent, surfactant, temperature, and humidity, we demonstrate the reproducible fabrication of homogeneous films of highly ordered PS beads on the cm^2 scale.

Optical and morphological characterization of highly ordered PS templates

These PS bead films are deposited on conductive transparent electrodes (*e.g.* FTO), which are useful for subsequent infilling by electrodeposition and for potential use of the resulting systems as active photoelectrodes. However, analogous PS opal films, exhibiting similar quality, were also successfully deposited on silicon, quartz, and copper substrates. While we have focused on the optimization of the process on FTO substrates, we have also performed the assembly on Cu foil. We have measured the surface roughness as the root mean square (RMS_{SR}) of FTO (RMS_{SR} = 13.2 nm) and Cu foil (RMS_{SR} = 26.0 nm) by means of atomic force microscopy (AFM, Fig. S9†). These two substrates have different, yet not dramatically so, surface roughnesses. However, the PS opal film formation works comparably well on both of them, as long as the substrate cleaning procedure (described in the Experimental section) is followed (Fig. 1 and S10†). We ascribe this effect to two possibly concomitant reasons: (1) the meniscus at the drying front plays a more significant role in the opal formation than the direct interaction of the PS beads with the substrate surface, and (2) the diameter of the PS beads is much larger than the actual roughness of the substrate, which consequently does not affect the assembly. The quality of the PS opal films can be seen by eye *via* the photonic effect, which manifests as a change of color in the transmission (Fig. 1b) and reflection (Fig. 1c) images of the films. To more thoroughly characterize the optical properties of the PS opal templates and assess their homogeneity over a large scale, we have conducted UV/Vis/NIR optical transmission and specular reflection measurements of the films, with results for PS beads with diameters 170, 200, 280, 350, 390, 400, 500, 510, and 600 nm shown in Fig. 2. A main photonic crystal stop band is observed in the reflection spectra (Fig. 2a), and is complemented by a dip in the transmission spectra (Fig. 2b).

The large amplitude and small full width at half maximum (FWHM) of these features in the optical spectra are indicative of the high quality, 3D nature, and large area of the PS opal films. As a measure of the quality factor of these opal structures, the FWHM values are reported in Table 1 and, to the best of our knowledge, correspond to some of the highest values published in the literature.[42,49] The broad increase in reflectance that occurs in the IR is due to the FTO substrate (Fig. S11†). When the same film is prepared on a quartz substrate, this reflectance disappears (Fig. S12†).

SEM images show the homogeneity of these structures over large scales and indicate that the sphere arrangement in the PS

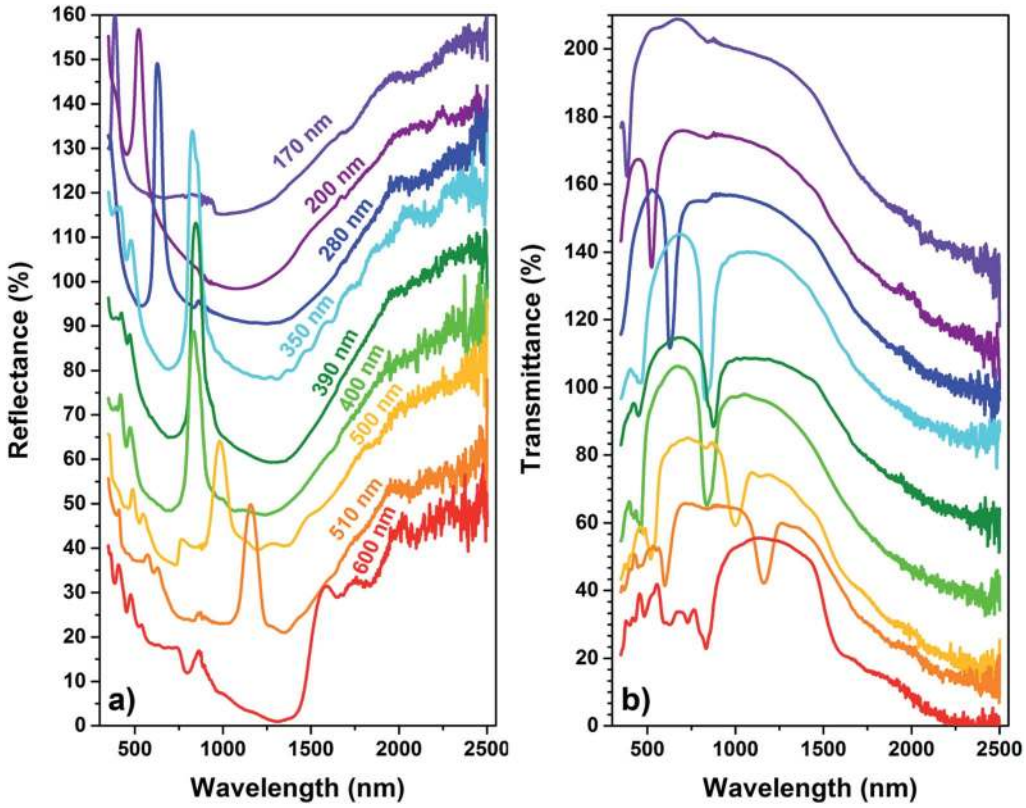

Fig. 2 (a) Spectral reflectance and (b) transmission spectra of the PS bead templates, showing a peak in reflectance and a dip in the transmission where the photonic gap is formed. The increase in the reflectance in the IR is from the FTO substrate (see Fig. S11†).

Table 1 FWHM values for opal films fabricated from various diameters of PS beads

Diameter (nm)	170	200	280	350	390	400	500
FWHM (nm)	36.1	52.9	44.9	65.6	71.0	84.2	80.5
FWHM (eV)	0.298	0.239	0.140	0.117	0.121	0.147	0.103

templates is FCC (Fig. 1a), which is consistent with prior reports of analogous systems.[32,33,50] In order to calculate the position of the photonic crystal stop band, the optical data have been compared to prediction based on the Bragg–Snell law (eqn (1)).[50] For an FCC assembly, the expected reflectance peak maximum can be calculated according to:

$$\lambda = \frac{2}{m}\left[\frac{\sqrt{2}}{\sqrt{h^2+k^2+l^2}}\right] D\sqrt{{n_{\text{avg}}}^2 - \sin^2\theta} \quad (1)$$

where λ is the wavelength of the PBG; m is the order of Bragg diffraction; h, k, and l are the Miller indices; D is the pore center-to-center distance (approximately bead size); n_{avg} is the average refractive index (1.44) for an FCC structure of polystyrene and air; and θ is the angle between the incident light and the normal of the substrate plane. n_{avg} takes into account the refractive index of polystyrene (1.59) and of air (1.00), as calculated in eqn (2) using the effective medium approximation, where f_{PS} and f_{air} are the volume fraction of PS and air, respectively.[51]

$$n_{\text{avg}} = f_{\text{PS}} n_{\text{PS}} + f_{\text{air}} n_{\text{air}} \quad (2)$$

A comparison of the calculated and measured PBG peak positions for each bead size is provided in Table 2, and highlights that the experimental photonic crystal stop bands for the different PS sizes are in reasonable agreement with the ones calculated with the Bragg–Snell law.

The Bragg–Snell model also predicts shifts of the PBG as a function of the incoming angle of the incident light. Therefore, reflectance measurements were performed as a function of angle in the range of 45–80° (in 5° increments) relative to the normal vector from the substrate surface (*i.e.* 10–45° from the substrate plane). Most of the films exhibit a main peak that red shifts as the PS diameter increases, suggesting that this feature is from the periodic order of the beads. PS beads of sizes 200, 280, 350, and 500 nm are reported in Fig. 3, with the remaining sizes in Fig. S13.† A blue shift is observed as the incident angle progresses from the substrate normal towards the substrate plane. This finding agrees with the peak shift determined from

Table 2 Calculated and measured PBGs of different PS bead diameters

Diameter (nm)	Calculated PBG (nm)	Measured PBG (nm)
170	398.8	386.5
200	469.2	522
280	656.9	627.5
350	821.1	827.5
390	914.9	846
400	938.4	836
500	1173.0	981
510	1196.4	1157.5
600	1407.6	1586

the model. The calculation of the shift in the position of the (111) peak is tabulated in Table S2.†

To gain a further understanding of these optical features, we have performed full field optical simulations of the 3D PS opal films on SiO_2 substrates. As predicted by the Bragg–Snell law, we see a dip in the transmission corresponding to the PBG at wavelengths correlated with the close-packed (111) lattice planes of the simulated FCC PS opal films (Fig. 4a–c). While at smaller PS bead sizes there is a slight mismatch between the experimental and calculated PBG positions likely due to the polydispersity of the as-received PS beads (Fig. 4a). A better correlation in these features can be seen at lower wavelengths for larger bead sizes (Fig. 4b and c). These peaks are due to features in the photonic band structure arising from resonant modes of the individual PS spheres as described by Mie scattering theory.[52] A full comparison of the PBG position for the full range of measured and simulated bead sizes is presented in Fig. 5.

Electrodeposition as the infilling method of PS templates for the synthesis of scalable, nanoporous (photo)electrocatalytic materials

Establishing a reproducible and homogeneous opal template size series lays the foundation for creating inverse opal materials *via* infilling deposition methods and subsequent removal of the beads *via* calcination or chemical dissolution. Sol–gel, spin-coating, capillary, and evaporative methods have been used as top-down approaches to producing inverse opal structures.[32,49,53,54] However, these techniques suffer from drawbacks such as minimal control over the inverse opal film thickness, a need for repeated infilling steps, an overcoat layer that subsequently needs removal *via* selective chemical etching, and a risk of blocking the pores during the course of the deposition due to the top-down nature of the methods.[55,56]

In contrast to the methods described above, the bottom-up electrodeposition approach has several advantages, including control of nucleation and growth *via* voltage/current, the ability to vary the film thickness using the same template *via* deposition time, and the potential to produce low-cost large area samples.[53] Electrodeposited materials are preferentially grown up from the substrate towards the surface. This characteristic is

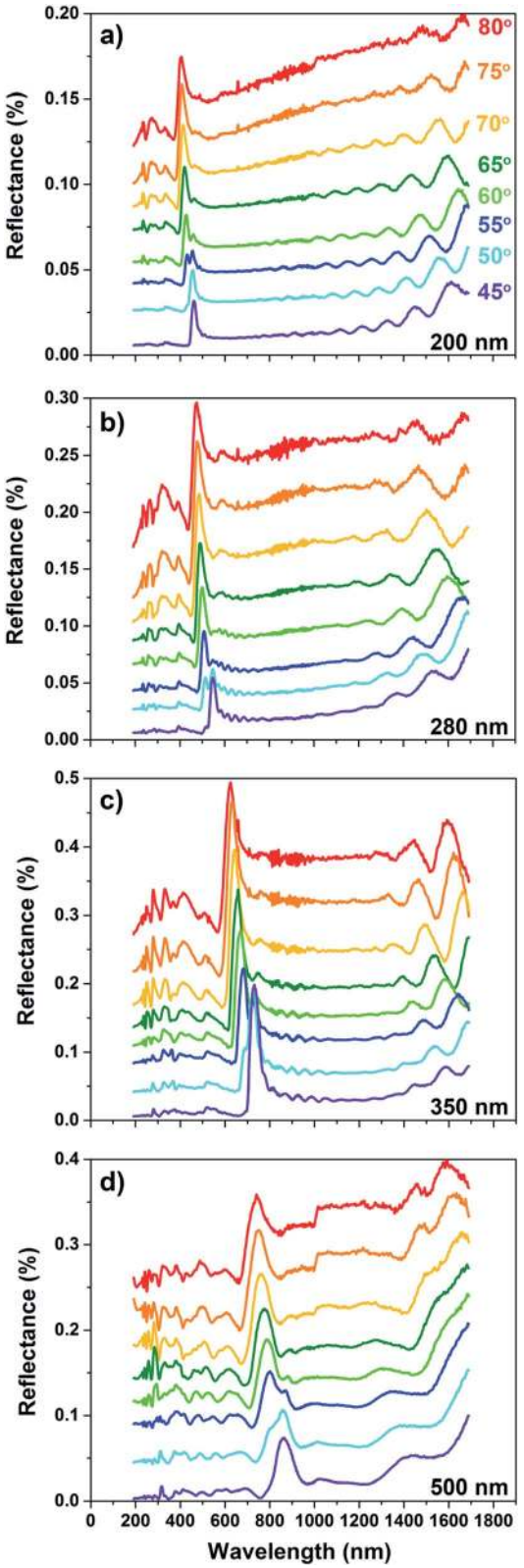

Fig. 3 Angle dependent reflectance data for PS templates of (a) 200, (b) 280, (c) 350, and (d) 500 nm diameters. The peak shifts from blue to red with increasing PS bead diameter, and from red to blue with increasing angle from the normal vector from the substrate.

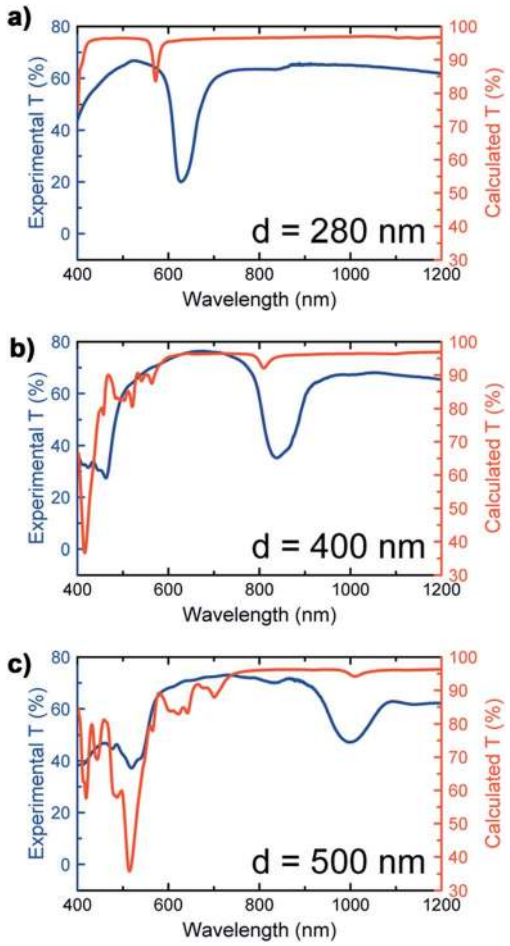

Fig. 4 Comparison of measured and simulated transmission of PS bead templates of (a) 280, (b) 400 and (c) 500 nm size under normal incidence plane wave illumination.

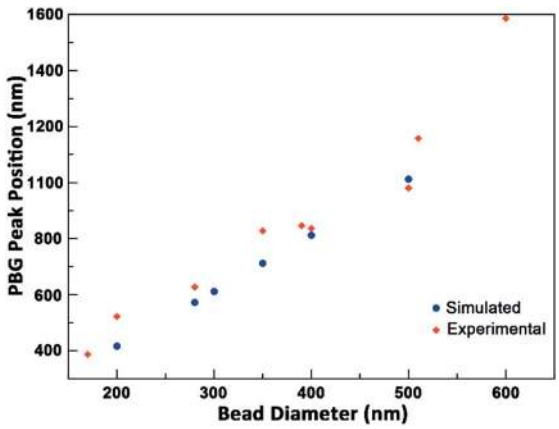

Fig. 5 Comparison of the position of the PBG for the full range of simulated and measured PS bead opals. The feature at the PBG was fitted with a Gaussian in order to extract its position.

particularly advantageous for enabling complete infiltration and filling of the interconnecting space between pores due to the outward growth in order to fabricate IO structures with good electrical contact and continuity.

We use our highly ordered PS bead films as templates for electrodepositing inverse opal electrodes. To demonstrate the versatility of this templating approach, we have chosen materials that cover the spectra of electrode materials of interest for solar fuel (photo)electrochemistry: Cu_2O (as an established photocathode), $BiVO_4$ (as an established photoanode), $CuBi_2O_4$ (as an emerging photocathode), and Cu (as an established catalyst for electrochemical CO_2 reduction). Cu_2O, $BiVO_4$, and $CuBi_2O_4$ absorb light in the visible range and have favorable band edge positions, which are beneficial properties for solar-driven photoelectrochemical water splitting or CO_2 reduction applications. However, they suffer from poor electron–hole separation yields and bulk recombination, which affect the activity[57] and stability of the materials,[4] particularly in planar systems. Therefore, synthetic nanostructuring approaches would benefit this class of transition metal oxide materials. In addition, the synthesis of nanostructured, porous Cu electrodes for CO_2 reduction has the potential to tune the kinetics of product selectivity due to CO_2 and reaction intermediate confinement in the pores. For example, the use of Ag-IOs has been recently studied to effectively tune efficiency and selectivity in CO_2 reduction.[58] Thus, we demonstrate how electrodeposition can be used as a bottom-up versatile infilling approach for different photoelectrocatalytic materials.

To fabricate the IO photonic crystals of the targeted materials, we have used PS templates of 500 nm beads for the Cu_2O and $BiVO_4$, 200 nm beads for $CuBi_2O_4$, and 280 nm beads for Cu. All the electrodeposition conditions used herein have been adapted from existing literature methods on electrodeposition of planar films of the corresponding materials (see the Experimental section for details). Tuning of the deposition time, temperature, and voltage/current can affect the growth rate and the quality of the films. Once electrodeposition of the desired material through the PS template is accomplished, the PS beads are removed *via* toluene/acetone immersion cycles, as in the case of Cu_2O and Cu, or *via* annealing, as in the case of $BiVO_4$ and $CuBi_2O_4$. After the removal of the PS beads, the resulting pore diameter is approximately 450 ± 15 nm for Cu_2O and $BiVO_4$, 212 ± 22 nm for $CuBiO_4$, and 213 ± 9 nm for Cu (Table S3 and Fig. S14†). In addition, the film thickness measured from the obtained IO films is approximately 900 nm for Cu_2O, 100 nm for $BiVO_4$, 42 nm for $CuBi_2O_4$, and 1.3 μm for Cu (Fig. S14 and Table S4†).

The SEM images of the final electrode films grown through the PS opal template are shown in Fig. 6. The Cu_2O films show a well-defined, multi-layered inverse opal structure (Fig. 6a), with a pore size slightly smaller (450 nm) with respect to the original PS bead size (500 nm). The film is relatively flat and oriented in the [111] direction from the substrate. The line-like discontinuities of the hexagonally patterned structure are a result of the grain boundaries present between grains in the PS opal template. Nevertheless, the registry of the structure is continuous between grains, and is observed over a large area as shown in Fig. S15.† Using electrodeposition as an infilling method for $BiVO_4$ results in an interesting, unexpected geometry: an inverse opal structure with a planar over-layer (Fig. S16†). In this case, the iridescence from the periodicity

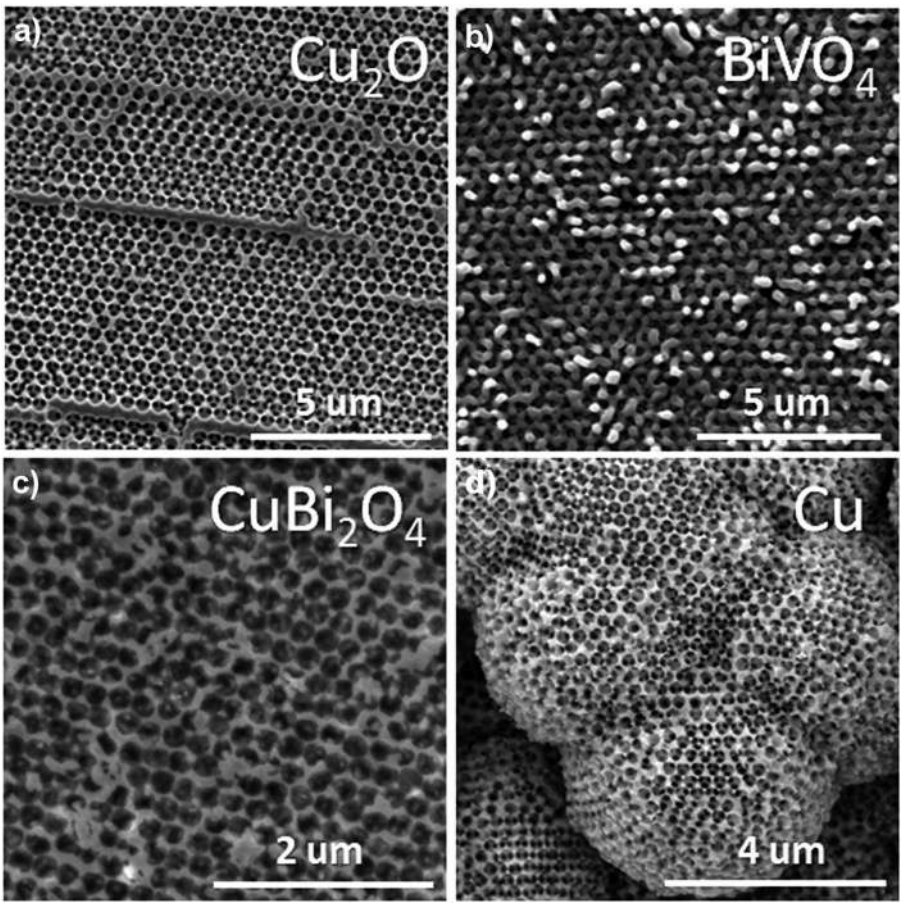

Fig. 6 SEM of (a) Cu_2O, (b) $BiVO_4$, (c) $CuBi_2O_4$, and (d) Cu inverse opal structures electrodeposited through PS opal templates.

of the inverse opal structure could be seen through the bottom of the substrate (Fig. S17†). When this overgrowth layer is gently removed *via* scotch tape, it reveals a patterned film that is the origin of the iridescence (Fig. 6b). This geometry is particularly attractive as removal of the photonic film with a conductive tape has been reported as a successful way to make electrode materials, and the presence of a planar over-layer, in contact with the tape, guarantees electrical contact through the film without preventing the use of our approach for the synthesis of (photo)electrocatalysts. The area of the patterned $BiVO_4$ covered virtually the entire substrate with crack-free areas to well over 1 mm^2 (Fig. S18†). The $CuBi_2O_4$ films also reflect the inverse opal structure (Fig. 6c). However, the quality of the films could be improved over a large scale (Fig. S19†). The presence of structural defects in the case of $CuBi_2O_4$ may be attributed to the inhomogeneous nature of the electrodeposition growth noted by Mullins and colleagues.[40] While Choi *et al.* have published an improvement upon this electrodeposition method, this approach involves using DMSO as a solvent and the PS beads are unstable in this environment over the time of the deposition.[59] Nevertheless, we report the first known demonstration of a $CuBi_2O_4$ inverse opal structure. Finally, the Cu film shows a pattern of spherical grain growth with uniform pores where the PS template was originally present (Fig. 6d). Despite the unusual grain growth, the order of the PS template is clearly maintained in the Cu film. The inverse opal structure is observed over a large scale as shown in Fig. S20.†

While the homogeneous deposition of patterned $BiVO_4$ and $CuBi_2O_4$ films was successful, further optimization of the deposition conditions for these ternary oxides is required to produce films of the same structural quality of the Cu_2O and Cu. In particular, nucleation and growth of these films plays an important role in achieving the desired quality and must be precisely controlled. For example, to improve the structural quality of Cu_2O and provide information on the growth mechanism, we have monitored its nucleation process in the opal template as a function of the deposition time (Fig. S21†). Shorter deposition times show that Cu_2O nucleates at individual PS beads. Then, prolonged deposition times show that Cu_2O encompasses the PS beads until it forms an over-layer. In addition, control and careful choice of voltage/current parameters, as well deposition temperature, have also been demonstrated to be important synthetic knobs.

To confirm that we have electrodeposited the targeted material in the presence of the PS template, we have conducted wide angle X-ray diffraction (XRD) experiments. The data shown in Fig. 7 confirm the cubic cuprite phase for Cu_2O, monoclinic

scheelite phase for $BiVO_4$, tetragonal kusachiite for $CuBi_2O_4$, and FCC for Cu with a small contribution from the (111) peak of Cu_2O as the surface is partially oxidized. These results are also in agreement with the modified electrodeposition procedures used herein.

In order to characterize the optical properties of these photonic crystal inverse opals, we have performed spectral reflectance measurements to assess the position of the photonic crystal stop band. As mentioned above, the presence of the PBG is determined by the refractive index of the material and the pore size of the opal replicas. Cu_2O is a high refractive index (2.7) material and therefore has the possibility of exhibiting a photonic band gap effect if the structure is well ordered. Fig. 8a shows the spectral reflectance of a Cu_2O inverse opal templated from a 500 nm PS film. By using the Bragg–Snell law, we can approximate the photonic crystal stop bands expected for an inverse opal structure of Cu_2O with a pore size of 450 nm. The results are 649 nm (220), 918 nm (200), and 1060 nm (111). These calculated peaks correlate well with the photonic crystal stop bands in the experimental data, which show a sharp peak at 625 nm and a broader peak at ~995 nm. The peak at 625 nm is relatively close to the calculated one (649 nm) for the (220) plane. The broader peak at ~995 nm could be a contribution from both the (111) and (200) planes. Notably, the appearance of these spectral features demonstrates that the high order of the inverse opal structure results in a photonic effect when compared to a planar film (Fig. S22†). This effect can be seen by eye as a yellow iridescence. Exhibition of a photonic effect from the Cu_2O film suggests that this material could be of interest as an active photocathode whose structure could additionally be used to tune how the incoming light interacts with the electrode. The spectral reflectance data of the $BiVO_4$ film with the overcoat layer removed are shown in Fig. S23.† Although a clear, angle dependent iridescence of the $BiVO_4$ films can be seen by eye, further improvement in the structural quality of the film is necessary to observe a defined photonic crystal stop band as exhibited by the Cu_2O inverse opal films. Similarly, the electrodeposition of $CuBi_2O_4$ needs further improvement to achieve uniformity over a large scale. Cu has a very low index of refraction, and thus it is not a good stand-alone candidate for the creation of a photonic effect.

Finally, even though functional characterization of these photoelectrodes is beyond the main focus of this paper, we have analyzed the performance of Cu_2O IOs as an active photoelectrode for CO_2 reduction. Upon illumination, the photogenerated electrons are present in the conduction band of Cu_2O, which lies energetically above the potentials for both CO_2 and H_2O reduction.[60] Thus, the energy level of the conduction band of Cu_2O is favorable to aid the photoelectrochemical reduction of CO_2 and generate a cathodic photocurrent. Fig. 8b reports the cathodic sweep for Cu_2O under aqueous conditions (0.1 M $KHCO_3$) in the presence of (and without) CO_2 in the dark and under illumination. While Cu_2O has been used for photoelectrocatalytic H_2 production,[61] direct photoelectrocatalytic CO_2 reduction with this material has yet to be demonstrated. Cu_2O inverse opals are tested in the presence of Ar, where CO_2

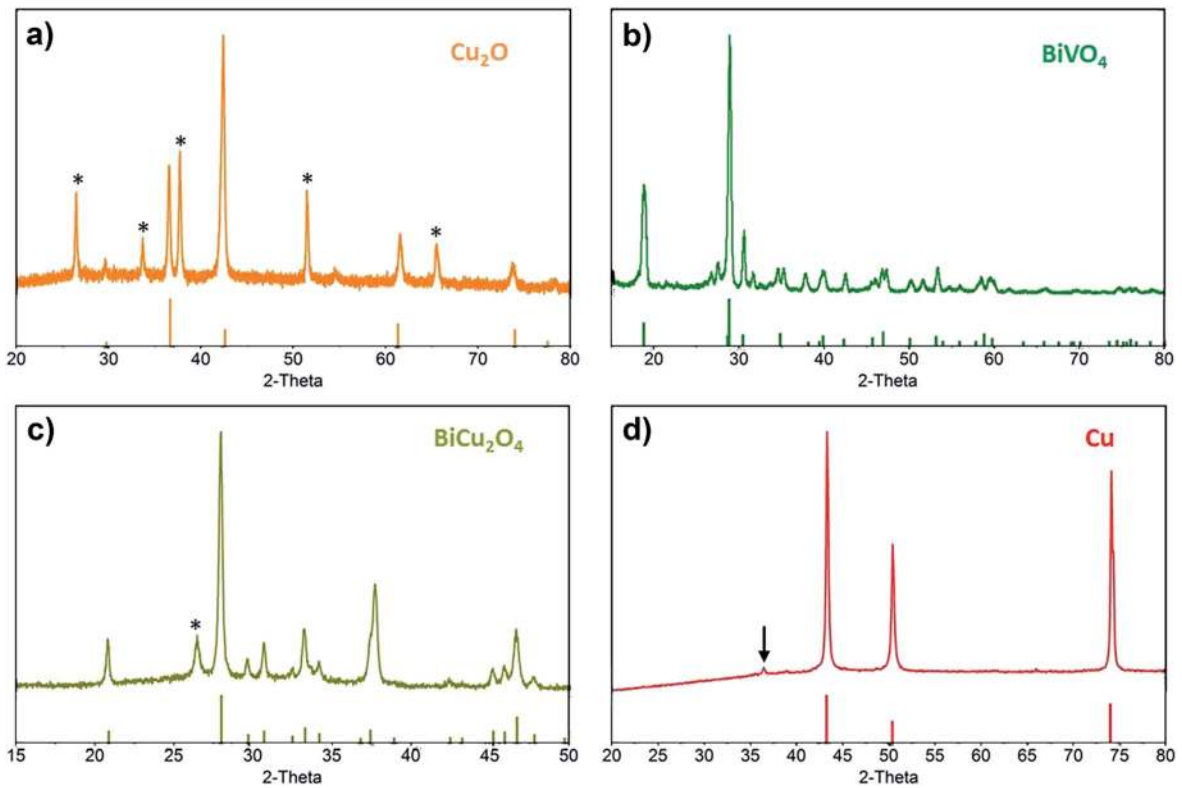

Fig. 7 XRD patterns of (a) Cu_2O, (b) $BiVO_4$, (c) $BiCu_2O_4$, and (d) Cu inverse opal structures. Asterisks mark peaks from the FTO substrate. The arrow in (d) marks the (111) plane for Cu_2O, indicating a minor presence in the Cu inverse opal.

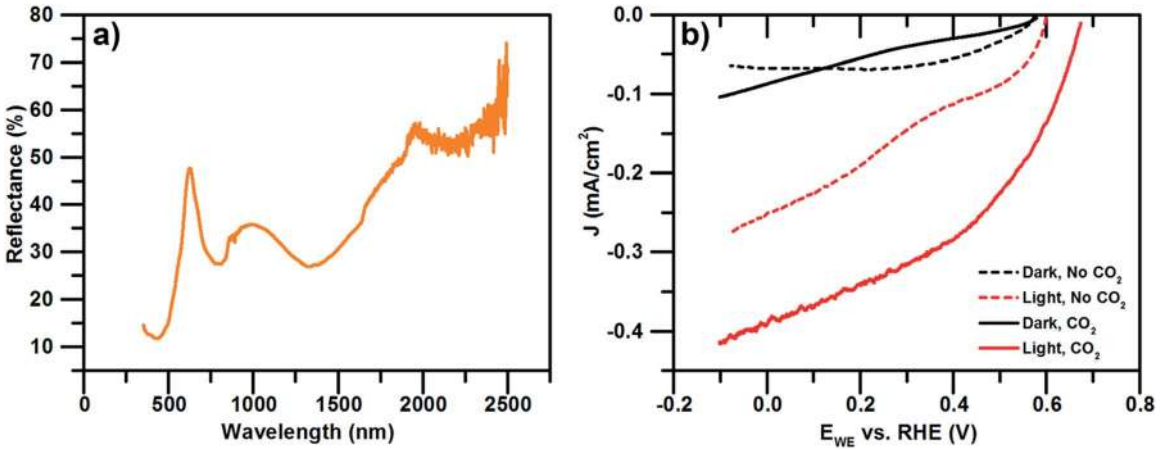

Fig. 8 A 500 nm Cu_2O inverse opal: (a) spectral reflectance spectrum showing two photonic features and (b) PEC curves under CO_2 reduction conditions in 0.1 M $KHCO_3$ electrolyte.

reduction is suppressed in favor of H_2 generation, and in the presence of CO_2, where H_2 generation and CO_2 reduction are competing with each other. Notably, an improvement in the onset potential (~0.1 V) and in the photocurrent (~0.39 mA cm^{-2} at 0 V *vs.* the RHE), together with an improvement in the fill factor are observed in the presence of CO_2, thus suggesting the potential of Cu_2O as an active photocathode for CO_2 reduction. Although Cu_2O is known to be unstable for long-term operation,[61] Cu_2O IOs are found to be sufficiently stable for the duration of the measurements presented here, as determined by measurements of several cyclic voltammograms (Fig. S24†). In addition, measurements of the incident photon-to-current efficiency (IPCE) as a function of wavelength, performed in the presence of CO_2 at 0.3 V *vs.* the RHE, reveal an onset near 620 nm (Fig. S25†). This value agrees well with the band gap of this material[61] and indicates that the photoexcitation of Cu_2O is indeed responsible for the cathodic photocurrent. While we consider this a preliminary result, and more thorough studies on stability and the role of pore size need to be performed, this finding demonstrates that our approach produces functional large scale materials for artificial photosynthesis.

Conclusions

In conclusion, we have reported the synthesis of scalable (cm^2), highly reproducible PS opal templates over a wide range of bead diameters, from 170 to 600 nm. We provide a careful analysis and discussion of the different parameters that play a role in the fabrication of these PS opal templates. The high quality of these PS opal templates is confirmed *via* optical transmission and reflectance measurements, where a strong photonic crystal stop band with a small FWHM is observed. The Bragg–Snell model is utilized to calculate the photonic crystal stop band of the PS opal template as a function of the PS bead size and as a function of the incident light, revealing that the calculated and experimental values are in good agreement with each other. In addition, finite difference time domain calculations of the optical response of PS opal films show that the calculated PBG is in good agreement with the experimental one. These high-quality opal substrates are used as templates for the electrodeposition of photoelectrocatalytic and electrocatalytic materials, thus providing a versatile and universal approach for producing highly periodic materials with pore size control over large areas. We show that Cu_2O, $BiVO_4$, $CuBi_2O_4$, and Cu IOs can be obtained by this approach, and confirm their identity by XRD. To the best of our knowledge, we report for the first time the electrodeposition of $BiVO_4$, and the synthesis of $CuBi_2O_4$ IO structures. Morphological and optical characterizations of the films show superior quality for the Cu_2O and Cu replicas, with the first demonstration of a photonic effect from Cu_2O IO synthesized in an all solution based approach. While optimization of the electrodeposition technique is still necessary and underway in our laboratory for the ternary oxide compositions, we show that this technique holds great promise for the fabrication of large scale opal templates and effectively converting them into equally homogeneous ordered replicas. Based on preliminary photoelectrochemical testing on Cu_2O photocathodes, we expect these structures to be promising in the field of CO_2 reduction. While we demonstrate the photoelectrochemical performance of Cu_2O IOs in reducing CO_2, the testing of these materials and the understanding of the effect of the pore size of the IO structure on (photo)electrocatalysis for CO_2 reduction is currently underway in our laboratory.

Acknowledgements

This study is based on work performed at the Joint Center for Artificial Photosynthesis, a DOE Energy Innovation Hub, supported through the Office of Science of the U.S. Department of Energy under Award Number DE-SC0004993. Lumerical simulations were done through a user proposal at the Molecular Foundry, supported by the Office of Science, Office of Basic Energy Sciences, of the U.S. Department of Energy under contract number DE-AC02-05CH11231. The AFM part of this work was supported by the Laboratory Directed Research and Development Program of Lawrence Berkeley National

Laboratory under U.S. Department of Energy contract number DE-AC02-05CH11231.

References

1 B. Parkinson, *ACS Energy Lett.*, 2016, **1**, 1057–1059.
2 C. John, O. Naomi, T. D. Peter, R. L. A. William, V. Bart, W. M. Ed, J. S. Carlton, L. Stephan, G. S. Andrew, A. G. Sarah, N. Dana, J. Peter, R. Mark, W. Bärbel, P. Rob and R. Ken, *Environ. Res. Lett.*, 2016, **11**, 048002.
3 B. Obama, *Science*, 2017, **350**, 1168–1169.
4 F. M. Toma, J. K. Cooper, V. Kunzelmann, M. T. McDowell, J. Yu, D. M. Larson, N. J. Borys, C. Abelyan, J. W. Beeman, K. M. Yu, J. Yang, L. Chen, M. R. Shaner, J. Spurgeon, F. A. Houle, K. A. Persson and I. D. Sharp, *Nat. Commun.*, 2016, **7**, 12012.
5 I. D. Sharp, J. K. Cooper, F. M. Toma and R. Buonsanti, *ACS Energy Lett.*, 2016, 139–150, DOI: 10.1021/acsenergylett.6b00586.
6 T. W. Kim and K.-S. Choi, *Science*, 2014, **343**, 990–994.
7 D. Kang, T. W. Kim, S. R. Kubota, A. C. Cardiel, H. G. Cha and K.-S. Choi, *Chem. Rev.*, 2015, **115**, 12839–12887.
8 G. Collins, E. Armstrong, D. McNulty, S. O'Hanlon, H. Geaney and C. O'Dwyer, *Sci. Technol. Adv. Mater.*, 2016, **17**, 563–582.
9 F. J. P. Schuurmans, D. Vanmaekelbergh, J. v. d. Lagemaat and A. Lagendijk, *Science*, 1999, **284**, 141–143.
10 A. Dutta, M. Rahaman, N. C. Luedi, M. Mohos and P. Broekmann, *ACS Catal.*, 2016, **6**, 3804–3814.
11 S. Sen, D. Liu and G. T. R. Palmore, *ACS Catal.*, 2014, **4**, 3091–3095.
12 X. Shi, K. Zhang and J. H. Park, *Int. J. Hydrogen Energy*, 2013, **38**, 12725–12732.
13 X. Zhang, Y. Liu, S.-T. Lee, S. Yang and Z. Kang, *Energy Environ. Sci.*, 2014, **7**, 1409–1419.
14 M. Zhou, J. Bao, Y. Xu, J. Zhang, J. Xie, M. Guan, C. Wang, L. Wen, Y. Lei and Y. Xie, *ACS Nano*, 2014, **8**, 7088–7098.
15 M. Zhou, H. B. Wu, J. Bao, L. Liang, X. W. Lou and Y. Xie, *Angew. Chem., Int. Ed.*, 2013, **52**, 8579–8583.
16 X. Chen, J. Ye, S. Ouyang, T. Kako, Z. Li and Z. Zou, *ACS Nano*, 2011, **5**, 4310–4318.
17 M. Ma, J. K. Kim, K. Zhang, X. Shi, S. J. Kim, J. H. Moon and J. H. Park, *Chem. Mater.*, 2014, **26**, 5592–5597.
18 A. F. Koenderink, A. Lagendijk and W. L. Vos, *Phys. Rev. B: Condens. Matter Mater. Phys.*, 2005, **72**, 153102.
19 B. Hatton, L. Mishchenko, S. Davis, K. H. Sandhage and J. Aizenberg, *Proc. Natl. Acad. Sci. U. S. A.*, 2010, **107**, 10354–10359.
20 J. I. L. Chen, G. von Freymann, V. Kitaev and G. A. Ozin, *J. Am. Chem. Soc.*, 2007, **129**, 1196–1202.
21 Y. H. Liu, D. Gokcen, U. Bertocci and T. P. Moffat, *Science*, 2012, **338**, 1327–1330.
22 C. Lupi, A. Dell'Era and M. Pasquali, *Int. J. Hydrogen Energy*, 2009, **34**, 2101–2106.
23 A. Ramirez, P. Hillebrand, D. Stellmach, M. M. May, P. Bogdanoff and S. Fiechter, *J. Phys. Chem. C*, 2014, **118**, 14073–14081.
24 Gunawan, W. Septina, S. Ikeda, T. Harada, T. Minegishi, K. Domen and M. Matsumura, *Chem. Commun.*, 2014, **50**, 8941–8943.
25 E. Fahrenkrug, J. S. Gu and S. Maldonado, *J. Am. Chem. Soc.*, 2013, **135**, 330–339.
26 D. Kang, T. W. Kim, S. R. Kubota, A. C. Cardiel, H. G. Cha and K. S. Choi, *Chem. Rev.*, 2015, **115**, 12839–12887.
27 J. Kim, H. S. Kim, J. H. Choi, H. Jeon, Y. Yoon, J. Liu, J. G. Park and P. V. Braun, *Chem. Mater.*, 2014, **26**, 7051–7058.
28 X. Li, Y. Jiang, Z. W. Shi and Z. Xu, *Chem. Mater.*, 2007, **19**, 5424–5430.
29 M. J. Deng, C. Z. Song, P. J. Ho, C. C. Wang, J. M. Chen and K. T. Lu, *Phys. Chem. Chem. Phys.*, 2013, **15**, 7479–7483.
30 M. Miyake, Y.-C. Chen, P. V. Braun and P. Wiltzius, *Adv. Mater.*, 2009, **21**, 3012–3015.
31 L. W. Zhang, C. Y. Lin, V. K. Valev, E. Reisner, U. Steiner and J. J. Baumberg, *Small*, 2014, **10**, 3970–3978.
32 G. I. N. Waterhouse and M. R. Waterland, *Polyhedron*, 2007, **26**, 356–368.
33 G. von Freymann, V. Kitaev, B. V. Lotsch and G. A. Ozin, *Chem. Soc. Rev.*, 2013, **42**, 2528–2554.
34 J. Du, X. Lai, N. Yang, J. Zhai, D. Kisailus, F. Su, D. Wang and L. Jiang, *ACS Nano*, 2011, **5**, 590–596.
35 L. Liu, S. K. Karuturi, L. T. Su and A. I. Y. Tok, *Energy Environ. Sci.*, 2011, **4**, 209–215.
36 N. Sultanova, S. Kasarova and I. Nikolov, *Acta Phys. Pol., A*, 2009, **116**, 585–587.
37 H. R. Philipp, in *Handbook of Optical Constants of Solids*, Academic Press, Burlington, 1997, pp. 749–763, DOI: 10.1016/B978-012544415-6.50038-8.
38 P. E. de Jongh, D. Vanmaekelbergh and J. J. Kelly, *Chem. Mater.*, 1999, **11**, 3512–3517.
39 J. A. Seabold and K. S. Choi, *J. Am. Chem. Soc.*, 2012, **134**, 2186–2192.
40 N. T. Hahn, V. C. Holmberg, B. A. Korgel and C. B. Mullins, *J. Phys. Chem. C*, 2012, **116**, 6459–6466.
41 D. Nagao, R. Kameyama, Y. Kobayashi and M. Konno, *Colloids Surf., A*, 2007, **311**, 26–31.
42 A. Chiappini, C. Armellini, A. Chiasera, M. Ferrari, L. Fortes, M. Clara Gonçalves, R. Guider, Y. Jestin, R. Retoux, G. Nunzi Conti, S. Pelli, R. M. Almeida and G. C. Righini, *J. Non-Cryst. Solids*, 2009, **355**, 1167–1170.
43 H. Yan, Y. Yang, Z. Fu, B. Yang, L. Xia, S. Fu and F. Li, *Electrochem. Commun.*, 2005, **7**, 1117–1121.
44 R. D. Deegan, O. Bakajin, T. F. Dupont, G. Huber, S. R. Nagel and T. A. Witten, *Nature*, 1997, **389**, 827–829.
45 H. Hu and R. G. Larson, *J. Phys. Chem. B*, 2006, **110**, 7090–7094.
46 L. Cui, J. Zhang, X. Zhang, L. Huang, Z. Wang, Y. Li, H. Gao, S. Zhu, T. Wang and B. Yang, *ACS Appl. Mater. Interfaces*, 2012, **4**, 2775–2780.
47 D. J. Norris, E. G. Arlinghaus, L. Meng, R. Heiny and L. E. Scriven, *Adv. Mater.*, 2004, **16**, 1393–1399.
48 S. Wong, V. Kitaev and G. A. Ozin, *J. Am. Chem. Soc.*, 2003, **125**, 15589–15598.

49 X. Zheng, S. Meng, J. Chen, J. Wang, J. Xian, Y. Shao, X. Fu and D. Li, *J. Phys. Chem. C*, 2013, **117**, 21263–21273.
50 R. C. Schroden, M. Al-Daous, C. F. Blanford and A. Stein, *Chem. Mater.*, 2002, **14**, 3305–3315.
51 W. L. Vos, R. Sprik, A. van Blaaderen, A. Imhof, A. Lagendijk and G. H. Wegdam, *Phys. Rev. B: Condens. Matter Mater. Phys.*, 1996, **53**, 16231–16235.
52 C. Vandenbem and J. P. Vigneron, *J. Opt. Soc. Am. A*, 2005, **22**, 1042–1047.
53 A. Stein, B. E. Wilson and S. G. Rudisill, *Chem. Soc. Rev.*, 2013, **42**, 2763–2803.
54 Z. Cai, J. Teng, Z. Xiong, Y. Li, Q. Li, X. Lu and X. S. Zhao, *Langmuir*, 2011, **27**, 5157–5164.
55 J. W. Galusha, C.-K. Tsung, G. D. Stucky and M. H. Bartl, *Chem. Mater.*, 2008, **20**, 4925–4930.
56 X. Chen, Z. Li, J. Ye and Z. Zou, *Chem. Mater.*, 2010, **22**, 3583–3585.
57 F. F. Abdi, L. Han, A. H. M. Smets, M. Zeman, B. Dam and R. van de Krol, *Nat. Commun.*, 2013, **4**, 2195.
58 Y. Yoon, A. S. Hall and Y. Surendranath, *Angew. Chem., Int. Ed.*, 2016, **55**, 15282–15286.
59 D. Kang, J. C. Hill, Y. Park and K. S. Choi, *Chem. Mater.*, 2016, **28**, 4331–4340.
60 S. N. Habisreutinger, L. Schmidt-Mende and J. K. Stolarczyk, *Angew. Chem., Int. Ed.*, 2013, **52**, 7372–7408.
61 A. Paracchino, V. Laporte, K. Sivula, M. Grätzel and E. Thimsen, *Nat. Mater.*, 2011, **10**, 456–461.